Ultrasound tomography in bone mimicking phantoms: Simulations and experiments

Timothe Falardeau and Pierre Belanger[a)]
Department of Mechanical Engineering, École de Technologie Supérieure, 1100 Notre-Dame Street West, Montreal, Quebec H3C1K3, Canada

(Received 9 February 2018; revised 29 October 2018; accepted 31 October 2018; published online 26 November 2018)

Bone quality assessment for osteoporosis diagnosis is usually performed using dual energy X-ray absorptiometry or X-ray quantitative computed tomography. Recent research demonstrated that both methods are inaccurate in diagnosing osteoporosis since they rely only on the bone mineral density. The literature on bone quantitative ultrasound suggests that ultrasonic waves are sensitive to multiple significant bone parameters such as mechanical properties, the bone volume fraction, and the micro-architecture. Typical ultrasound tomography techniques are limited to image objects with a low speed of sound contrast relative to a background medium. In this study, the possibility of adapting a more advanced ultrasound inversion technique referred to as the hybrid algorithm for robust breast ultrasound tomography for velocity mapping of bone mimicking phantoms was examined. The cortical bone thickness and the cortical bone speed of sound, which are directly related to the bone elastic properties, are parameters strongly correlated with the overall bone quality. A finite element model and an experimental test bench were developed to adapt the hybrid algorithm for robust breast ultrasound tomography to bone quality assessment. Although artefacts were present in the images generated, the results obtained enabled discrimination of a healthy bone phantom over an osteoporotic bone phantom based on the cortical bone thickness and the average cortical bone velocity. The speed of sound inside the cortical region of the bone phantoms was underestimated by 9.38% for the osteoporotic phantom, and by 10.68% for the healthy phantom relative to the values supplied by the bone phantom manufacturer, but there was a difference of 3.97% between the two samples. The difference between the measured cortical bone thickness of the reconstructed image and the X-ray computed tomography images was on average 0.4 mm.
© *2018 Acoustical Society of America*. https://doi.org/10.1121/1.5079533

[GH] Pages: 2937–2946

I. INTRODUCTION

Osteoporosis is a medical condition characterized by bone mass loss and micro-architectural property deterioration. People affected by osteoporosis have an increased risk of bone fracture, and thus this condition would ideally be diagnosed in its early stages to avoid complications. Li *et al.*[1] showed that the most common diagnostic tool, the dual-energy X-ray absorptiometry (DXA), is ineffective in diagnosing osteoporosis since the detection rate is as low as 17.1%. Li *et al.*[1] also showed that the second most common evaluation method, X-ray quantitative computed tomography (QCT), increased the detection rate to 46.3% but is more expensive, generates higher radiation doses and is still based only on the bone mineral density (BMD). Numerous studies[2–7] have pointed out that a model combining multiple bone characteristics (such as the bone cortical thickness, the density, the bone volume fraction and the mechanical properties) would be ideal for estimating the risk of fracture with a high degree of precision. Laugier and Haïat[8] showed that quantitative ultrasound (QUS) is sensitive to multiple bone properties such as the macro- and micro-architecture, porosities, and mechanical properties. QUS techniques are also generally less expensive than X-ray based ones, and are radiation-free. Axial transmission velocity measurements on the wrist and broadband ultrasonic attenuation (BUA) on the finger phalanxes and heel are the most prevalent QUS parameters examined for osteoporosis diagnosis. These measurements can be used in conjunction with X-ray QCT to evaluate the bone cortical thickness, but most of the advantages gained by using ultrasound instead of X-rays are then lost.

The two most common tomographic inversion methods are straight ray time-of-flight (TOF) tomography and diffraction tomography (DT). In hard tissues like bone, ultrasonic wave refraction is too important to consider that rays are travelling in straight paths for TOF tomography,[9] and standard DT cannot be used since the phase change through the bone is too big for the first-order Born or Rytov approximation to hold. The possibility of using a higher-order Born approximation, referred to as the distorted Born iterative method (DBIM), for bone ultrasound tomography, was investigated on children's bones in Ref. 10. Although most of the morphological features were represented correctly, the reconstructed image was not sufficiently accurate to quantify the cortical thickness and the average cortical velocity. Another relatively new ultrasound imaging method, the full wave inversion (FWI),[11,12] has enabled velocity mapping of

[a)]Electronic mail: pierre.belanger@etsmtl.ca

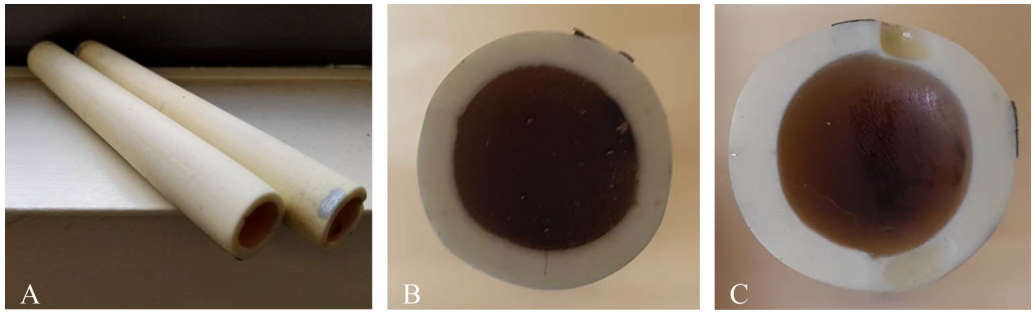

FIG. 1. (Color online) (A) True phantom solutions human bone mimicking phantoms, (B) cross-section of the healthy bone phantom, and (C) cross-section of the osteoporotic bone phantom.

objects with high speed of sound (SOS) contrast relative to the background medium. Bernard *et al.*[13] achieved good SOS maps of a realistic tibia-fibula numerical model. However, no experimental validation has yet been done on bones or bone phantoms using FWI. Furthermore, a forward model must be computed for FWI, resulting in time consuming and computationally expensive calculations.

A faster way to image high velocity contrast materials relative to the background using ultrasound was proposed by Huthwaite and Simonetti[14] for velocity mapping of breast tissues. This algorithm is referred to as the hybrid algorithm for robust breast ultrasound tomography (HARBUT). In HARBUT, a low resolution bent-ray TOF tomography (BRT)[15] is first used as a background for beamforming (BF). Then, a filter is convolved with the resulting image to obtain a high-resolution DT image. Initial *in vivo* experiments on breast tissues[16] suggest that HARBUT could provide more accurate reconstructions than DT and higher resolution than BRT.

The aim of this study is to evaluate the possibility of using an adapted HARBUT for velocity mapping in bone mimicking phantoms with a view to developing a method for detecting osteoporosis. The main objective was to compare the velocity maps of osteoporotic and healthy bone mimicking phantoms using a circular array of transducers. Section II describes the algorithm, the bone phantoms, the finite element (FE) model, as well as the experimental setup. The results are then presented and discussed in Sec. III. Finally conclusions are drawn in Sec. IV.

II. MATERIALS AND METHODS

A. Description of the bone phantoms

Human bone tissue is a multi-scale, anisotropic, heterogeneous, porous, and highly attenuating medium.[17] Attenuation is one of the main limiting factors of bone ultrasound tomography since it is frequency-dependent.[18] Biological tissues are considered to be viscoelastic since they return to their original shape and size when deformed, but are subject to viscous losses.[19] This energy dissipation mechanism due to the relaxation phenomenon, is the primary causes of absorption in soft tissues. In hard tissues, attenuation is more complex. Boundary reflections and other absorption mechanisms, such as mode conversion, anisotropy loss, porosity, crack friction, and fluid motion, are responsible for attenuation in solids.[20–22]

In this study, True Phantom Solutions[23] bone mimicking phantoms with homogenized properties were used to facilitate the development of the imaging algorithm without the constraints of using cadaveric samples. The bone phantoms consisted of cortical bone mimicking shells filled with a viscoelastic material that has an ultrasonic attenuation representative of the total attenuation of trabecular bone, as shown in Fig. 1. The viscoelastic material however does not capture the scattering effect of trabecular bone. The material used to make the bone phantom is a proprietary mix of epoxy resin with alumina powder. The mechanical properties of the bone phantoms were provided by the manufacturer and are detailed in Table I. The geometrical properties of the bone are shown in Fig. 2.

In the trabecular region of the bone mimicking phantoms, absorption was much stronger than in water or in the cortical region since it is a highly viscous medium. The trabecular region medium is semisolid although it was simplified to an attenuative acoustic medium with the same SOS as water in the FE model described in Sec. II B, since its behavior is much closer to that of a fluid than of a solid. Even though the attenuation does not play a significant role in the speed of sound tomography, the values for the attenuation in the bone phantom are in line with the values from literature.[24–26] Although the speed of sound of the cortical region is somewhat lower than the values from the literature.[27] Therefore, the results presented in this paper remain valid, as the aim is to estimate the speed of sound difference between two bones of similar velocity.

B. FE model

A FE model was designed in ABAQUS 6.13 to simulate wave propagation inside the bone phantoms. The sample

TABLE I. Acoustic properties of the bone mimicking phantoms supplied by True Phantom Solutions.

	Density (g/cm^3)	Velocity at 1 MHz (m/s)	Attenuation at 1 MHz (dB/cm)
Cortical healthy bone phantom	2.33	2900	3.5
Cortical osteoporotic bone phantom	2.15	2750	5.0
Trabecular healthy bone phantom	1.66	1700	40
Trabecular osteoporotic bone phantom	1.39	1600	30

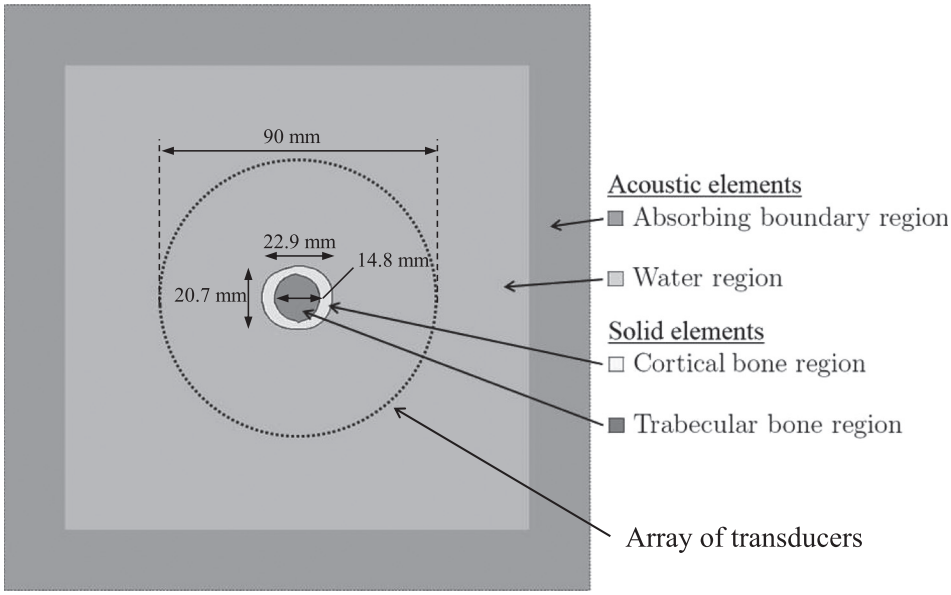

FIG. 2. Ultrasound tomography configuration used in the FE model. The dotted line around the bone phantom represents the position of the array of transducers.

was immersed in water at 20 °C to provide a couplant between the probe and the bone phantom. The FE model was reduced to 2D in order to reduce the size of the model and the simulation time. Moreover, since the waves are transmitted through the bones, it is assumed that only a small quantity of energy would leak in the other direction. However, this remains a source of error. In this study, a circular array ultrasound tomography configuration was chosen to map the velocity inside the bone mimicking phantoms. The circular array configuration is the only transducer arrangement that provides a full view of the object to image. Moreover, polar coordinates can be used to reduce the algorithm complexity and computation time. The bone phantom geometry was extracted from an X-ray micro-computed tomography (μCT) scan. The configuration used in this study is presented in Fig. 2.

In Fig. 2, the dots surrounding the bone mimicking phantom represent the 360 emitter (point sources) and receiver positions on a circle of 90 mm diameter. Fewer dots are represented than in the actual configuration to help visualize the circular array configuration. A five cycle Hann windowed 500 kHz toneburst was sent and captured from all point source positions in a pitch–catch manner to obtain the full send–receive TOF data.

An input file was used to generate the nodes location of the point sources in water and to mesh the square elements of the model. The element size and integration time steps for convergence of the numerical results were 20 elements per wavelength and 20 time step integrations per period.[28]

The pressure field was calculated for each point source by running successive simulations at every emission position. The simulation time of a single point source on a single core running at 2.4 GHz was approximately 1.5 h. However when running an asymmetric model, all 360 point sources are required for a total simulation time of approximately three weeks. All materials were considered isotropic and homogeneous. Acoustic impedance properties were implemented as boundary conditions at the fluid–solid interfaces with a tie constraint to couple both surfaces. Absorbing boundaries consisting of acoustic elements with exponentially increasing volumetric drag (as shown in Fig. 2) were included to simulate an infinite water tank.[29] The absorbing boundary region, the water region and the trabecular region were modeled with quadrilateral acoustic elements. The cortical region was modeled with quadrilateral solid elements with an isotropic elastic modulus set to match the True Phantom Solutions osteoporotic cortical bone SOS. In the cortical and trabecular regions, the attenuation was modeled, respectively, as Rayleigh damping[30] and volumetric drag.[31] At high frequency, the β coefficient associated with stiffness damping is dominant over the α coefficient associated with mass damping.[32] Therefore, only the β coefficient of Rayleigh damping was included in the FE model to simplify coefficient estimation. The Rayleigh damping β and volumetric drag γ coefficients were estimated experimentally by matching attenuation measurements on rectangular bone phantom samples of a thickness of 15 mm at 2.25 and 1 MHz with the coefficients' values. The amplitude decay of multiple backwall echoes were compared with the model. The measurements were repeated three times. The β and γ values were, respectively, found to be 2 e-8 s^{-1} and 1e7. The attenuation could not be measured at 500 kHz due to the extent of the time domain signal at this frequency.

In this study, the FE model simulation plane was defined as the xy plane. Only bulk waves were of interest in the imaging algorithm, thus guided waves propagating around the cortical bone shell were not analyzed in depth. In fluids, shear motion is not sustained, and only pressure waves, more commonly referred as L-waves, are supported. At a fluid–solid interface, mode conversion occurs since both S-waves and L-waves exist in solids. When considering 2D propagation, the shear vertical wave does not couple to other modes since there are no waves propagating in the yz or xz planes. Wave propagation considering only the first reflection at the fluid–solid boundary is shown in Fig. 3.

In this study, only the arrival time of the solid L-waves converted into fluid L-waves is of interest for the tomographic reconstruction. The wave of interest is represented

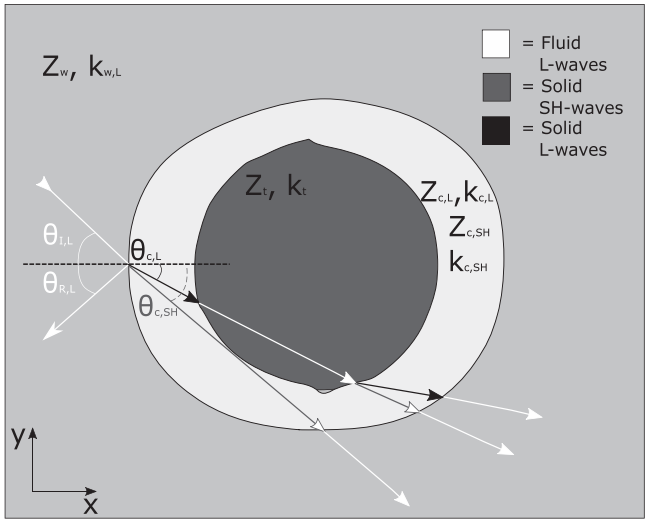

FIG. 3. Wave propagation considering only transmitted waves in the bone phantom.

as the top white arrow on the right of Fig. 3. It was demonstrated in the literature[33,34] using simulations and experiments that the ultrasonic guided waves are always arriving before the bulk waves. Signal processing detailed in Sec. II D will be used to evaluate the TOF of the mode of interest.

C. Experimental setup

1. Test bench configuration

The setup used to validate the FE results was an ultrasound tomography test bench with two single element Olympus V323-SM 2.25 MHz ultrasound immersion transducers attached to stepper motors in a water tank (Fig. 4). The stepper motors were mounted on an aluminum ring which enables the rotation of the transducers around the sample in order to replicate a full circular array configuration. The advantage of using this method is that a virtually unlimited number of transduction positions can be used. This solution comes with drawbacks such as a longer acquisition time and more position variations in measurements, but greatly reduces fabrication costs for the research and development of an ultrasound tomography system.

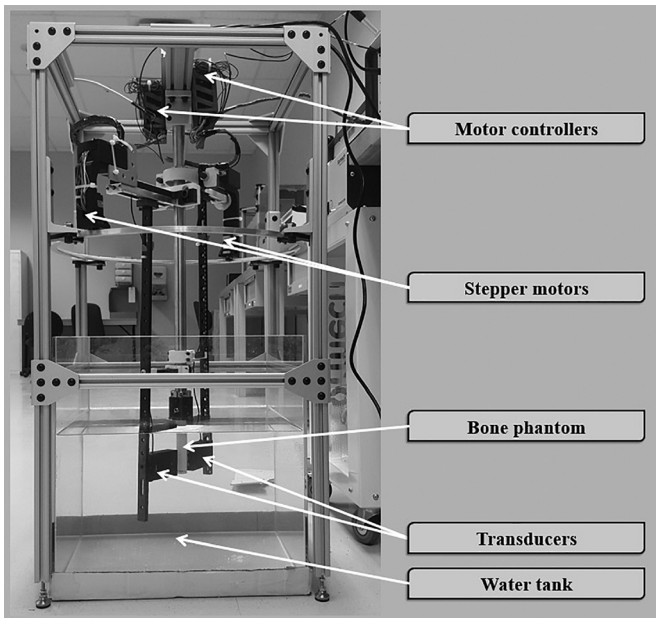

FIG. 4. Experimental ultrasound tomography test bench.

Data acquisition was automated using Matlab and a TiePie Handyscope HS5. A Falco Systems WMA-300 5 MHz 150V amplifier was used to increase the signal amplitude in order to penetrate through the sample and obtain a sufficient signal-to-noise ratio (SNR) for arrival time extraction.

In this study, 322 emission positions and 243 reception positions were used. The angle of reception was limited to 272° so as to avoid contact between the emitting and receiving transducers, as represented in Fig. 5. This arrangement represents a compromise between the total acquisition time and the sampling resolution. The emitted signals were coded using Golay coded sequences to increase the SNR. Golay coded sequences were used to increase the SNR for a limited acquisition time.

D. Description of the algorithm

1. HARBUT algorithm

Imaging of diffracting objects, such as bones, is limited to a restricted range of tomographic methods. DT using the first-order Born or Rytov approximation is the most common method for mapping the velocity inside diffracting media. When imaging materials for which the phase change through the object relative to the background medium is much greater than π, both approximations do not hold.[35] More advanced imaging techniques, such as DBIM or FWI, must be used to solve this inverse scattering problem using prior knowledge of a scattering model or a background close to the real object. HARBUT is a fast and robust ultrasound tomography algorithm for imaging diffracting media with high SOS contrast relative to the background medium. In HARBUT, a BRT low-resolution velocity map is used as an initial background for BF. The BF image is then filtered in the frequency domain to obtain a high-resolution DT image.[36] The algorithm can be iterated to reduce errors and

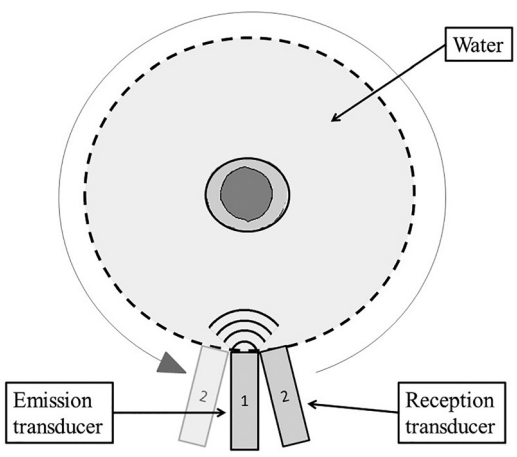

FIG. 5. Simplified top view representation of the experimental ultrasound tomography test bench.

total phase change between iterations.[37] A schematic of the HARBUT algorithm is presented in Fig. 6. As detailed in Ref. 37, the HARBUT algorithm splits the object function into two components,

$$O(\mathbf{r}) = O_b(\mathbf{r}) + O_p(\mathbf{r}), \tag{1}$$

where $O(\mathbf{r})$ is the object function at location $\mathbf{r}$, $O_b(\mathbf{r})$ is the known background object and $O_p(\mathbf{r})$ is the perturbation object. In HARBUT, the initial background object $O_b(\mathbf{r})$ is calculated through the TOF BRT. The aim of the initial background is to reduce the phase change between the background and the perturbation object so as to respect the Born approximation when computing the diffraction tomography image. The HARBUT algorithm implements diffraction tomography by filtering a beamforming image as detailed in Ref. 36. Standard beamforming using the difference between the wavefield measured by the array and the background wavefield is used. The perturbation object function $O_p(\mathbf{r})$ is then obtained by multiplying the Fourier transform beamforming image with

$$\frac{|\Omega|\sqrt{4k_u^2 - |\Omega|^2}}{16\pi^2 \exp\dfrac{i\pi/4}{\sqrt{8\pi k_u}}}, \tag{2}$$

where Ω is the 2D frequency value and $k_u = \omega/c_b$ is the background wavenumber defined by the speed of the sound c_b of the background medium.

The major advantage of using HARBUT over FWI is that the former allows faster computation. The BRT background only takes a few seconds as compared to a forward model computation, which can range from a few hours to several days, depending on the number of parameters taken into account, the number of receiving positions in the field, and the method used (analytical model, finite difference, or finite elements). The computation of the HARBUT algorithm for a given image was in the region of a few minutes. The other advantage of HARBUT is that no prior knowledge of the object characteristics and properties is necessary. This feature is convenient for medical imaging since bone geometrical features and properties can vary considerably between patients.

In the first application of HARBUT proposed by Huthwaite *et al.*, the SOS and density contrast were always below 10% relative to the background medium. Therefore, the phase change caused by the velocity contrast was moderately above π and the density gradient was not taken into account. In this study, the velocity and the density in the cortical region was far from the background medium (see Table I), and thus the total phase change was over 12π between the propagation through the bone and in the background and the density gradient was significant at the fluid–solid boundary. Therefore, an alternate data post-processing algorithm was developed to improve the imaging results.

2. Data post-processing

Multiple data post-processing algorithms have been proposed for HARBUT. The reconstruction accuracy strongly depends on the algorithm used to extract the TOF and the frequency data. In the context of bone ultrasound tomography, multiple modes are superposed in the time traces: (1) ultrasonic guided waves propagating around the circumference of the bone and (2) bulk shear and longitudinal waves propagating through the bone. More details were provided on the modes superposed in the time traces in Sec. II B. A typical experimental time-gated time trace is shown in Fig. 7. In this time trace, the ultrasonic guided wave packet and longitudinal bulk wave packet are well separated in time. For other pairs of transducers the wave packets are interfering.

In this study, the method used to extract the TOF as well as the frequency component of the longitudinal wave propagating through the bone combined thresholding and the automatic TOF picker based on the Akaike information criterion (AIC).[38,39] The extraction of TOF was done in three steps. First, the global maximum of the signal was located using the Hilbert transform in a given time domain signal. Second, the first local maximum arriving after the ultrasonic guided wave packet propagating around the circumference was located by setting a threshold equal to a fraction of the global maximum. The fraction value was calculated by dividing the smallest bulk wave amplitude from the maximum amplitude of the time trace. In the third step, the time of the first local maximum and the global maximum were used as the time limit of the window parameter for the automatic AIC TOF picker. The algorithm was finally iterated by reducing the size of the scanning window by using the minimum time limit as the time value obtained by AIC TOF. Selecting the right scanning window is essential for a precise BRT reconstruction since errors in the arrival time estimation lead to

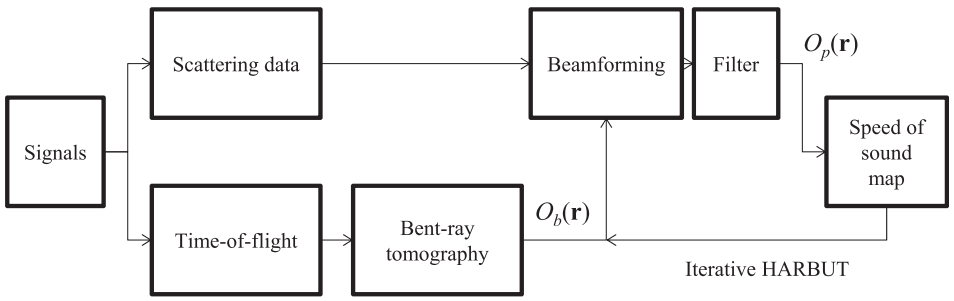

FIG. 6. Schematic of the HARBUT algorithm. From the time domain signals, the TOF of the mode of interest as well as the scattering data are extracted. The TOF is used to generate an initial low-resolution bent-ray tomography algorithm. This low-resolution image is used as a background to the beamforming algorithm. The beamforming image is then filtered to generate a speed of sound map. The beamforming algorithm is then iterated by using the speed of sound map from the previous iteration as the background in the beamforming.

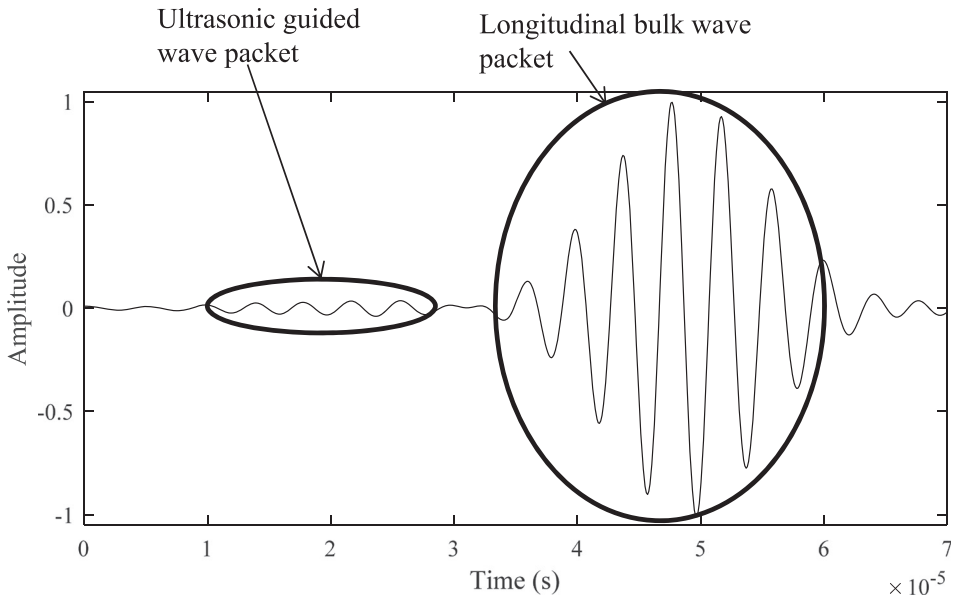

FIG. 7. A typical experimental time trace between source position 1 and sensor position 90. In this configuration the ultrasonic guided wave packet and the longitudinal bulk wave packet are well separated in time.

artefacts. This method yields a closer approximation of arrival times than both methods used separately. In this study, iterating the AIC TOF algorithm 3 times provided sufficiently accurate results for the BRT reconstruction.

The post-processing algorithm also used a wave mode separator by curvature analysis of the Hilbert transform. When two or more waves arrive close together in time, the automatic AIC TOF picker is often unable to separate the contribution of waves. In this study, when bulk compressional waves travelled close to the edge of the object, the wave travelling in water only could superpose with the bulk wave transmitted through the object and water. In all cases when the bulk wave packets transmitted through the object and water superposed with the bulk wave packets transmitted in water only, the arrival time estimated by the AIC TOF picker was slower. One way to overcome this problem is to take advantage of the information contained in the Hilbert transformed signal. When a single pulse is received on a transducer, the envelope of the signal contains a certain signature holding information such as its width and slope. When two wave packets are received close together in time, the appearance of the envelope changes: the width increases, and an inflexion point appears. This means that the curvature or second-order derivative of the enveloped signal contains a minima within the half-width or half-period of the transmitted toneburst. This minima can be found by performing thresholding on the second-order derivative of the windowed Hilbert transformed time trace smoothed by multiple moving averages, as shown in Fig. 8.

Frequency components were extracted by applying a fast Fourier transform on the bandpass filtered time traces windowed around the TOF calculated for BRT. Windowing the signal reduced the noise level, but eliminated scattered components associated with finer details. The frequency components were normalized such that the maximum frequency components received on the diagonal of the scattering matrix would be equal to 1. This process was done experimentally by positioning the receiving transducer directly in front of the transmitting transducer.

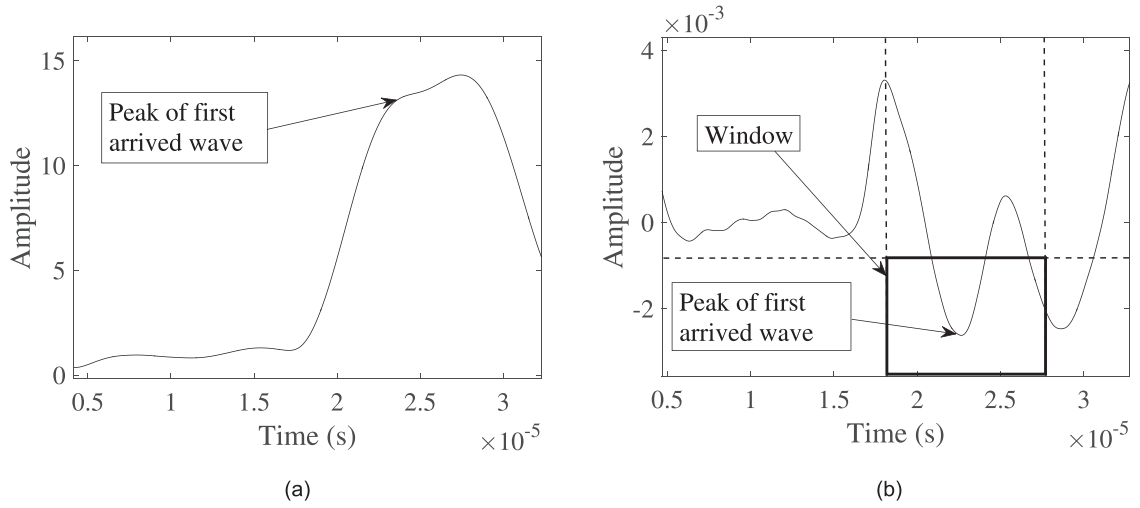

FIG. 8. Hilbert transform of a time domain signal containing (a) two wave packets close together in time and (b) its second derivative.

III. RESULTS AND DISCUSSION

A. Comparison between FE and experiments

FE and experimental velocity maps of the osteoporotic bone phantom reconstructed using the adapted HARBUT are presented in Fig. 9.

Here, the diameter of the circles represents the average diameters of the bone phantom since it is not a perfect cylinder. In Fig. 9(a), the average velocity of the cortical shell and trabecular region was estimated, respectively, at 2771 and 1548 m/s, with errors of 0.76% and 4.32% from the values set in the FE model. In Fig. 9(b), the average velocity was estimated at 2492 m/s in the cortical shell and 1548 m/s in the trabecular region, with errors, respectively, of 9.38% and 6.50% from True Phantom Solutions values. Both methods' results fall within a 10% relative error, and replicate the true bone phantom geometry with a good precision. The main difference between the FE velocity map and the experimental velocity map lies in the SOS variation within the cortical shell. The maximum difference between the true cortical bone velocity and the cortical bone velocity in the FE map was close to 20%. In the reconstruction of the experimental results, the maximum difference increased to 25%. This increase in variation was likely caused by the differences between the FE model and the experimental setup. In the FE model, the pressure field was generated by point sources, whereas when using the experimental test bench, the field was generated by two Olympus V323-SM transducers. The Olympus V323-SM transducer has a nominal element diameter of 6 mm. At 500 kHz the corresponding near field length is 3.04 mm and the distance between the bone phantom surface and the transducers was approximately 35 mm. The aperture of the transducers strongly affected the generated field. The transducers used experimentally were directive, and did not behave like point sources. When the received signal amplitude dropped due to directivity, the BRT reconstruction quality was degraded since the TOF extraction algorithm was less effective when the signal amplitude was close to the noise amplitude.

B. Comparison between CT and experiments

In Fig. 10, the BRT (a) and (b) and the HARBUT (c) and (d) velocity maps of the bone phantoms using the experimental test bench results are presented. The (e) and (f) images show the corresponding μCT scans.

1. Cortical thickness measurements

The advantage of using HARBUT over BRT only in velocity mapping can be seen by comparing Fig. 10(a) to Fig. 10(c) and Fig. 10(b) to Fig. 10(d). While BRT yields morphological features and SOS close to the true object, HARBUT further enhances the final image since it can account for diffraction effects. This characteristic enables the detection of finer details since scattering occurs when the size of a heterogeneity is in the same order of magnitude as the wavelength of the transmitted wave. Although the cortical and trabecular bone regions of the BRT images were easily distinguishable, only the HARBUT images were adequate for evaluation of the cortical thickness. These images matched the true bone phantoms' geometry with a maximum error in cortical thickness evaluation of less than 2 mm and an average error of 0.4 mm. The porosities of the osteoporotic bone phantom were smaller than the Born approximation resolution limit ($\lambda/2$). Therefore, the porosities are not visible in the HARBUT image, although there is a local SOS decrease. The cortical thickness value was evaluated using image segmentation methods. A circular Hough transform was applied on the HARBUT image to estimate the radius and center of the object. Using this information, the cortical and trabecular region were separated by combining a Canny edge detector and a threshold. The threshold was set in order to eliminate high velocity artefacts far from the boundaries. Figure 11 shows how the osteoporotic bone and the cortical bone regions are segregated using this method. The cortical bone thickness is determined as the distance between the internal and the external edges, following a straight line from the center.

2. Accuracy of the velocity maps

As mentioned earlier, the average velocity of the osteoporotic bone mimicking phantom was evaluated at 2492 m/s in the cortical region, with an error of 9.38%, and at 1704 m/s in the trabecular region, with an error of 6.50%. The average velocity of the healthy bone mimicking phantom was

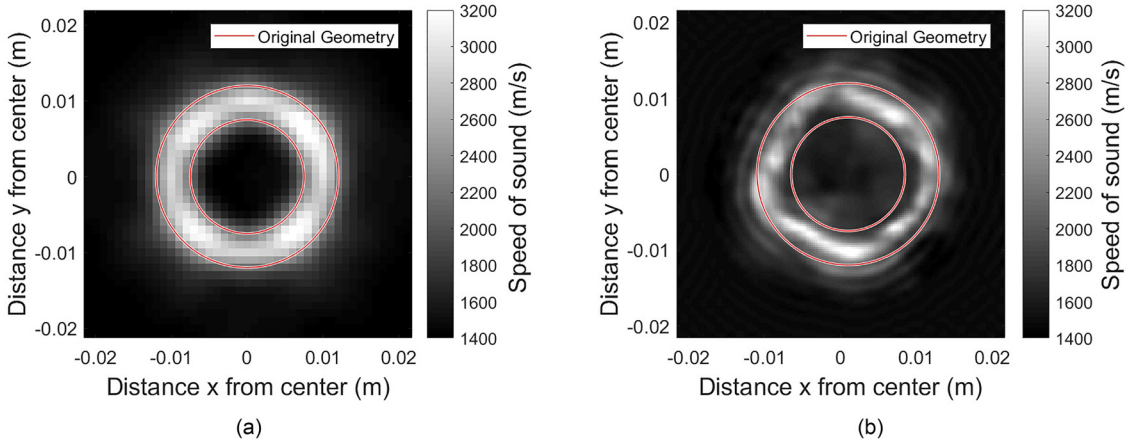

FIG. 9. (Color online) (a) FE and (b) experimental velocity map of the osteoporotic bone phantom using the adapted HARBUT algorithm.

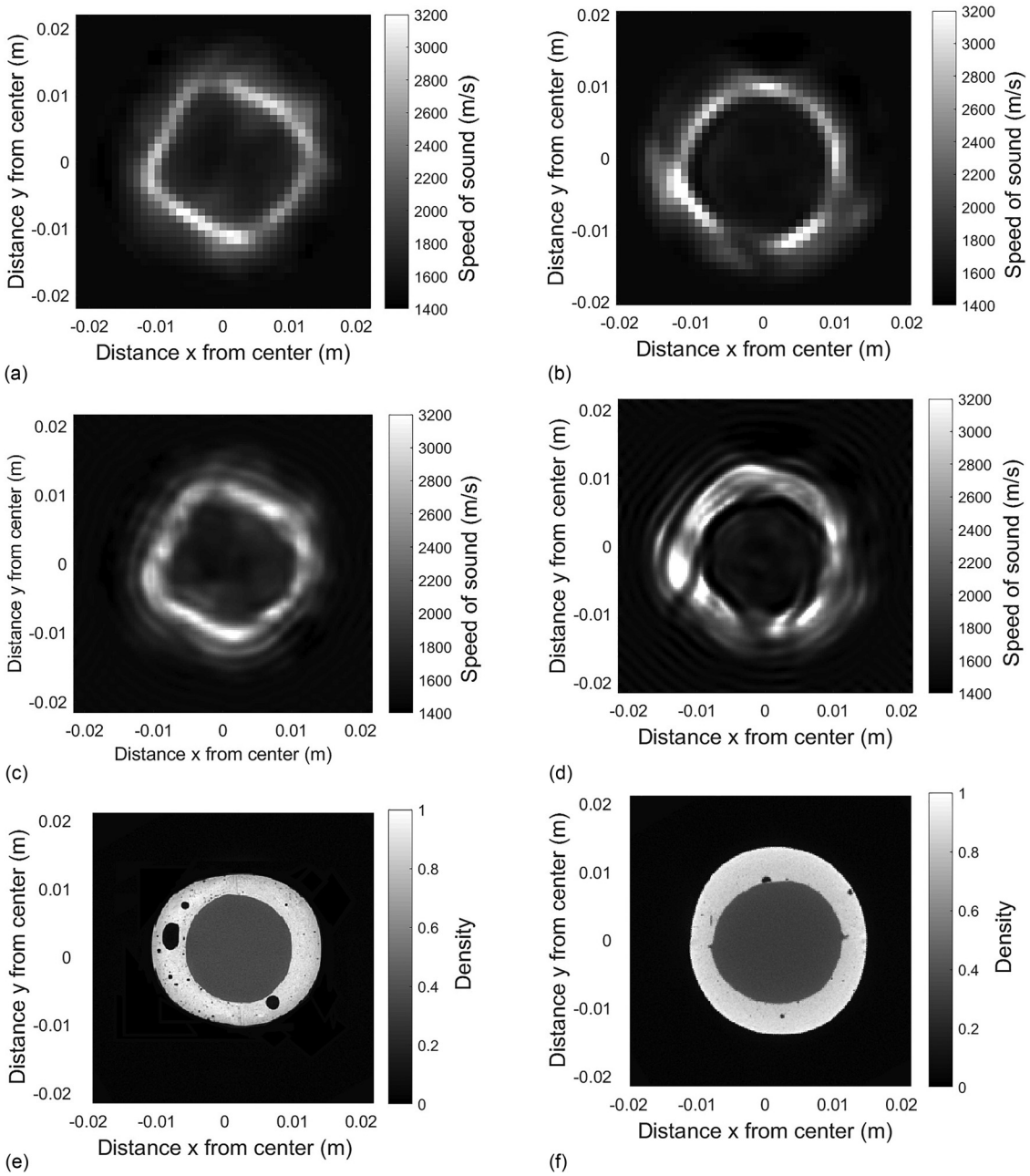

FIG. 10. Velocity maps of the osteoporotic (a) and (c) and the healthy (b) and (d) bone mimicking phantom using 322×322 emission-reception positions processed with the BRT algorithm only (a) and (b) and with the iterative HARBUT algorithm (c) and (d). (e) and (f) Density maps obtained using μCT for the osteoporotic and healthy bone, respectively. The μCT images were obtained in the same measurement plane as the ultrasonic tomography.

evaluated at 2591 m/s in the cortical region, with an error of 10.66%, and at 1578 m/s in the trabecular region, with an error 7.18%. The velocity in the center of both cortical shells was close to the expected value although the average velocity was lower than the values provided by True Phantom Solutions (see Table I). The healthy bone phantom is still distinguishable from the osteoporotic bone phantom since there is an average SOS difference of 99 m/s, corresponding to 3.97%, between the two.

The average velocity was underestimated in the cortical region since the 3D effects, the density gradient and the attenuation were not accounted for in the DT part of the HARBUT algorithm. These deviations are more significant at boundaries due to the high density gradient at the water–cortical bone and cortical bone–trabecular bone interfaces. The attenuation caused by the out-of-plane scattering and energy dissipation mechanisms in the material also decreased SOS values since the amplitude is lower than expected when the waves go through the bone phantom. The combined artefacts underestimated the velocity, and were more significant at boundaries, leading to lower accuracy in the image segmentation and a lower average SOS value in the cortical region.

The SOS map of the trabecular regions did not allow a distinction between the two bone phantoms. The average trabecular velocity of the osteoporotic bone phantom was higher than in the healthy bone phantom, whereas the opposite should have been expected. This difference is strongly correlated with artefacts generated by the BRT algorithm. In

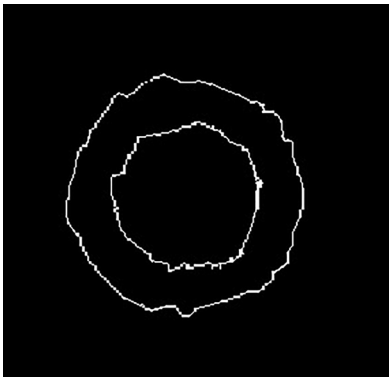

FIG. 11. Binary mapping of the osteoporotic bone phantom edges.

Fig. 10(a), artefacts were present inside and outside the object, whereas in Fig. 10(c), they were only present in the water. The higher SOS in the trabecular region of the osteoporotic bone phantoms caused by the artefacts increased the average SOS value and reduced the accuracy of the image segmentation. These errors were generated in the data post-processing algorithm when the arrival times were not correctly evaluated. This is currently the main limitation of the proposed method and further work must be done in order to obtain velocity maps closer to the real object properties.

IV. CONCLUSION

In this study, the possibility of using an adapted HARBUT was evaluated for velocity mapping with a view to developing a method for detecting osteoporosis. The HARBUT algorithm was adapted by combining thresholding, AIC and curvature analysis based on the Hilbert transformed time trace.

The morphological features of the reconstructed images were always within 2 mm of the true bone phantom geometry. The cortical thickness was evaluated by combining a circular Hough transform, a Canny edge detector, and a threshold of the HARBUT images. A difference of 99 m/s, corresponding to 3.97%, in the average velocity of the cortical shells of the bone phantoms, allowed a discrimination between a healthy bone phantom and an osteoporotic bone phantom, although values were approximately 10% lower than the True Phantom Solutions values provided. Errors in the average velocities of the trabecular regions of the bone phantom were always below 10%. Artefacts generated in the BRT background from erroneous TOF estimations were the main cause of errors in the HARBUT images.

Overall, HARBUT is a significant improvement over standard ultrasound TOF and DT, but further work must to be done to improve the accuracy of the TOF extraction algorithm. Incorporating a map of the density gradient in the object function and compensating attenuation could also be investigated as a way to correct velocity underestimation in the DT algorithm.

ACKNOWLEDGMENTS

This work was developed in collaboration between Centre de recherche l'Hôpital du Sacré-Coeur de Montréal and École de technologie supérieure and was funded by Professor Belanger NSERC Discovery grant.

[1]N. Li, X. M. Li, L. Xu, W. J. Sun, X. G. Cheng, and W. Tian, "Comparison of QCT and DXA: Osteoporosis detection rates in postmenopausal women," Int. J. Endocrinol. **2013**, 895474.
[2]J. A. Kanis, D. Black, C. Cooper, P. Dargent, B. Dawson-Hughes, C. De Laet, and L. Melton, "A new approach to the development of assessment guidelines for osteoporosis," Osteoporosis Int. **13**(7), 527–536 (2002).
[3]A. N. Law, A. M. Bollen, and S. S. U. K. Chen, "Detecting osteoporosis using dental radiographs: A comparison of four methods," J. Am. Dent. Assoc. **127**(12), 1734–1742 (1996).
[4]M. Muller, P. Moilanen, E. Bossy, P. Nicholson, V. Kilappa, J. Timonen, M. Talmant, S. Cheng, and P. Laugier, "Comparison of three ultrasonic axial transmission methods for bone assessment," Ultrasound Med. Biol. **31**(5), 633–642 (2005).
[5]V. Egorov, A. Tatarinov, N. Sarvazyan, R. Wood, L. Magidenko, S. Amin, S. Khosla, R. J. Ruh, J. M. Ruh, and A. Sarvazyan, "Osteoporosis detection in postmenopausal women using axial transmission multi-frequency bone ultrasonometer: Clinical findings," Ultrasonics **54**(5), 1170–1177 (2014).
[6]O. Nackaerts, R. Jacobs, H. Devlin, S. Pavitt, E. Bleyen, B. Yan, H. Borghs, C. Lindh, K. Karayianni, P. Van der Stelt, E. Marjanovic, J. E. Adams, and K. Horner, "Osteoporosis detection using intraoral densitometry," Dentomaxillofacial Radiol. **37**(5), 282–287 (2008).
[7]A. Sarvazyan, A. Tatarinov, V. Egorov, S. Airapetian, V. Kurtenok, and C. J. Gatt, "Application of the dual-frequency ultrasonometer for osteoporosis detection," Ultrasonics **49**(3), 331–337 (2009).
[8]P. Laugier and G. Haïat, *Bone Quantitative Ultrasound* (Springer, Dordrecht, 2011), Vol. 576.
[9]P. Belanger, P. Cawley, and F. Simonetti, "Guided wave diffraction tomography within the born approximation," IEEE Trans. Ultrason., Ferroelectr., Freq. Control **57**(6), 1405–1418 (2010).
[10]P. Lasaygues, J. P. Lefebvre, R. Guillermin, V. Kaftandjian, J. P. Berteau, M. Pithioux, and P. Petit, "Advanced ultrasonic tomograph of children's bones," in *Acoustical Imaging* (Springer, Dordrecht, 2012), pp. 31–38.
[11]J. Wiskin, D. T. Borup, Q. S. Johnson, M. Berggren, T. Abbott, and R. Hanover, "Full-wave, non-linear, inverse scattering," in *Acoustical Imaging* (Springer, Dordrecht, 2007), pp. 183–193.
[12]J. Rao, M. Ratassepp, and Z. Fan, "Guided wave tomography based on full waveform inversion," IEEE Trans. Ultrason., Ferroelectr., Freq. Control **63**(5), 737–745 (2016).
[13]S. Bernard, V. Monteiller, D. Komatitsch, and P. Lasaygues, "Ultrasonic computed tomography based on full-waveform inversion for bone quantitative imaging," Phys. Med. Biol. **62**(17), 7011–7035 (2017).
[14]P. Huthwaite and F. Simonetti, "High-resolution imaging without iteration: A fast and robust method for breast ultrasound tomography," J. Acoust. Soc. Am. **130**(3), 1721–1734 (2011).
[15]A. Hormati, I. Jovanovic, O. Roy, and M. Vetterli, "Robust ultrasound travel-time tomography using the bent ray model," in *Medical imaging 2010: Ultrasonic Imaging, Tomography, and Therapy* (2010), Vol. 7629, pp. 76290I.
[16]P. Huthwaite, F. Simonetti, and N. Duric, "Combining time of flight and diffraction tomography for high resolution breast imaging: Initial *in vivo* results," J. Acoust. Soc. Am. **132**(3), 1249–1252 (2012).
[17]V. Sansalone, S. Naili, V. Bousson, C. Bergot, F. Peyrin, J. Zarka, J. D. Laredo, and G. Haiat, "Determination of the heterogeneous anisotropic elastic properties of human femoral bone: From nanoscopic to organ scale," J. Biomech. **43**(10), 1857–1863 (2010).
[18]M. J. T. M. Cloostermans and J. M. Thijssen, "A beam corrected estimation of the frequency dependent attenuation of biological tissues from backscattered ultrasound," Ultrason. Imag. **5**(2), 136–147 (1983).
[19]K. K. Shung, *Diagnostic Ultrasound: Imaging and Blood Flow Measurements* (CRC, Boca Raton, FL, 2005).
[20]D. H. Johnston, M. N. Toksöz, and A. Timur, "Attenuation of seismic waves in dry and saturated rocks: II. Mechanisms," Geophysics **44**(4), 691–711 (1979).
[21]E. Bossy, F. Padilla, F. Peyrin, and P. Laugier, "Three-dimensional simulation of ultrasound propagation through trabecular bone structures measured by synchrotron microtomography," Phys. Med. Biol. **50**(23), 5545–5556 (2005).

[22]K. A. Wear, "Mechanisms for attenuation in cancellous-bone-mimicking phantoms," IEEE Trans. Ultrason., Ferroelectr., Freq. Control **55**(11), 2418–2425 (2008).
[23]A. Wydra and R. G. Maev, "A novel composite material specifically developed for ultrasound bone phantoms: Cortical, trabecular and skull," Phys. Med. Biol. **58**(22), N303–N319 (2013).
[24]M. Sasso, G. Haïat, Y. U. Yamato, S. Naili, and M. Matsukawa, "Dependence of ultrasonic attenuation on bone mass and microstructure in bovine cortical bone," J. Biomech. **41**(2), 347–355 (2008).
[25]M. Sasso, G. Haïat, Y. U. Yamato, S. Naili, and M. Matsukawa, "Frequency dependence of ultrasonic attenuation in bovine cortical bone: An *in vitro* study," Ultrasound Med. Biol. **33**(12), 1933–1942 (2007).
[26]G. Haïat, F. Padilla, F. Peyrin, and P. Laugier, "Variation of ultrasonic parameters with microstructure and material properties of trabecular bone: A 3D model simulation," J. Bone Miner. Res. **22**(5), 665–674 (2007).
[27]H. Sievänen, S. Cheng, S. Ollikainen, and K. Uusi-Rasi, "Ultrasound velocity and cortical bone characteristics *in vivo*," Osteoporosis Int. **12**, 399–405 (2001).
[28]F. Moser, L. J. Jacobs, and J. Qu, "Application of finite element methods to study transient wave propagation in elastic wave guides," in *Review of Progress in Quantitative Nondestructive Evaluation* (Plenum, New York, 1998), pp. 161–167.
[29]A. H. Nielsen, "Absorbing boundary conditions for seismic analysis in ABAQUS," in *Proc. of the 2006 ABAQUS Users Conference* (2006).
[30]R. E. Spears and S. R. Jensen, "Approach for selection of Rayleigh damping parameters used for time history analysis," J. Pressure Vessel Technol. **134**(6), 061801 (2012).
[31]H. Li, G. Zhang, G. Chen, and L. P. Jing, "Laboratory experiment and computer simulation of ultrasonic wave propagation in fractured and inhomogeneous rock," in *Alaska Rocks 2005, The 40th U.S. Symposium on Rock Mechanics (USRMS)*, American Rock Mechanics Association (2005).
[32]A. Zerwer, G. Cascante, and J. Hutchinson, "Parameter estimation in finite element simulations of Rayleigh waves," J. Geotech. Geoenviron. Eng. **128**(3), 250–261 (2002).
[33]Q. Grimal, D. Rohrbach, J. Grondin, R. Barkmann, C. C. Gluer, K. Raum, and P. Laugier, "Modeling of femoral neck cortical bone for the numerical simulation of ultrasound propagation," Ultrasound Med. Biol. **40**(5), 1015–1026 (2014).
[34]R. Barkmann, P. Laugier, U. Moser, S. Dencks, M. Klausner, F. Padilla, G. Haiat, M. Heller, and C. C. Gluer, "*In vivo* measurements of ultrasound transmission through the human proximal femur," Ultrasound Med. Biol. **34**(7), 1186–1190 (2008).
[35]A. C. Kak and M. Slaney, *Principles of Computerized Tomographic Imaging* (IEEE, New York, 1988), pp. 203–273.
[36]F. Simonetti and L. Huang, "From beamforming to diffraction tomography," J. Appl. Phys. **103**(10), 103110 (2008).
[37]P. Huthwaite and F. Simonetti, "High-resolution guided wave tomography," Wave Motion **50**(5), 979–993 (2013).
[38]C. Li, L. Huang, N. Duric, H. Zhang, and C. Rowe, "An improved automatic time-of-flight picker for medical ultrasound tomography," Ultrasonics **49**(1), 61–72 (2009).
[39]X. Zhang, J. Fincke, A. Kuzmin, V. Lempitsky, and B. Anthony, "A single element 3D ultrasound tomography system," in *Engineering in Medicine and Biology Society (EMBC) 37th Annual International Conference of the IEEE* (2015).